Influence of carbon nanotubes on microstructure and corrosion performance of additively manufactured 316L stainless steel

Venkata Bhuvaneswari Vukkum [a, *], Jijo Christudasjustus [a, b], Troy Y. Ansell [c], Andy Nieto [c], Rajeev Kumar Gupta [a, **]

[a] Department of Materials Science and Engineering, North Carolina State University, Raleigh, NC, USA

[b] Physical and Computational Sciences Directorate, Pacific Northwest National Laboratory, Richland, WA, USA

[c] Coatings and Composites for Extreme Environments (CE)^2 Laboratory, Department of Mechanical and Aerospace Engineering, Naval Postgraduate School, Monterey, CA, 93943

** Corresponding author, vvukkum@ncsu.edu

* Corresponding author, rkgupta2@ncsu.edu

Highlights

1. Laser powder bed fusion of CNT-modified 316L stainless steel feedstock
2. Enhanced pitting corrosion resistance due to the feedstock modification by CNT
3. Pitting corrosion resistance evaluated at room temperature, 35 and 50 ℃
4. The altered microstructure-corrosion relationship due to CNT addition

Abstract

Laser powder bed fusion (LPBF) was performed on feedstock-modified 316L stainless steel powder with 1 and 2 vol% carbon nanotubes (CNT). The corrosion resistance was evaluated following cyclic potentiodynamic polarization tests conducted in 0.6 M NaCl at room temperature, 35 and 50 ℃, and immersion tests in 6 % $FeCl_3$. The CNT addition has increased the pitting potential and decreased number of pits formed during immersion in $FeCl_3$ solution, which could be attributed to Mn-Si-O nano inclusions refinement and segregation of chromium around the inclusions. The observed corrosion behavior was correlated with the altered microstructure due to CNT addition.

Keywords

Additive Manufacturing, Laser powder bed fusion, corrosion, stainless steel, feedstock, carbon nanotubes

1 Introduction

Additive manufacturing (AM) is an advanced manufacturing technique that can replace conventional manufacturing techniques like casting, forging, welding, and rolling [1–5]. Additive manufacturing technologies have several advantages, like fabricating complex structures, printing complicated compositions, design freedom, and producing macro to micro size components in a single step following a layer-by-layer process. Laser powder bed fusion (LPBF) is a trending metal additive manufacturing (AM) technique that was often used to print austenitic stainless steel, such as 316L [3,4,6]. Austenitic 316L stainless steel has several applications ranging from kitchenware to aerospace, medical and nuclear industries [3,7–10]. Implementing AM techniques to produce metallic components can revolutionize the manufacturing sector and the application of materials. The three-dimensional metal parts produced by LPBF are fabricated by spreading a thin layer of metal powder on a build platform called powder bed and, later, using a high-power laser to selectively melt and fuse the powder particles in a layer-by-layer process. As each layer solidifies, the build platform is lowered, and the process is repeated until the entire component is built. The feedstock powders on the powder bed experience extreme temperatures (~2000-3727 °C) and rapid solidification rates (~10^4-10^8 K/s) during the LPBF process [11–13]. The major disadvantage of LPBF printed 316L stainless steel is inconsistency in properties like corrosion resistance which is attributed to the manufacturing defects such as porosity, cracks, residual stress, and surface roughness [14–21] and atypical microstructure such as melt pools and melt pool boundaries, cellular and sub-cellular structures, solute segregation along the cellular boundaries, dislocations, and oxide nano inclusions [17,22–28]. Several researchers have adopted an emerging feedstock modification strategy that could overcome the limitations and improve corrosion resistance of iron, aluminum and magnesium alloys [29–38]. Incorporating a suitable additive like W [39], Ag [40], and Carbon nanotubes (CNT) [41–43], $La(NO_3)_3.6H_2O$ [44], CrN [27], TiB_2 [30], CeO_2 [44,45], and Y_2O_3 [46] to the 316L primary feedstock has been reported in the literature. Many researchers focus on enhancing the mechanical properties, and only a few researchers aim to improve the corrosion resistance of laser powder bed fusion printed 316L stainless steel (LPBF-316L) [27,39]. There are several methods (1) the straightforward blending of additive and primary alloy powders [47], (2) depositing the additive onto the surface of the primary alloy powders through a coating process [48], (3) utilizing mechanical alloying techniques such as ball milling is employed to achieve a homogenous mixture of additive and primary alloy powders [27], and (4) the process of

gas atomization where the primary alloy powders along with the additive are directly produced during atomization [49], to perform the feedstock modification. Many researchers opted for feedstock modification performed via mechanical alloying like ball milling of primary feedstock powder and additive [21,27,30,42,45,50–54]. The external additive added alters the microstructure resulting in altering the alloy properties.

The corrosion performance of 316L stainless steel (SS) has been hugely dependent on the microstructure acquired by the manufacturing processes. Generally, the 316L SS manufactured using conventional manufacturing techniques has γ-austenitic phase with manganese sulphide (MnS) inclusions in the microstructure [55]. These deleterious MnS inclusions of size above 0.7 µm act as cathodic particle and initiate corrosion in the anodic γ-austenitic steel matrix [56,57]. A thorough literature review shows no evidence of MnS inclusions in LPBF-316L but the presence of oxide inclusions that ranged from several tens of nanometers to several hundred of nanometers [3,28,58]. Here are few examples where researchers reported different size of oxide nano inclusions i.e., 30-50 [27], 40-80 nm [59], 50 nm [55], 100 nm [60], 30-140 nm [61], and 2-5µm [62]. Researchers had reported different composition of oxide nano inclusions like Mn-Si-O [17,25], Mn-Si-S-O [27], Mn-Al-Si-N-O [55], Si-Cr-Ni-Fe-O [24], Si-Mn-Al-O [63] , Cr-Si-O [64], Fe-Cr-Ni-Mn-Mo-Si-O [28] and Cr-Ni-Mn-Si-O [25] but their influence on corrosion performance has not been extensively studied. The density, chemical composition and size of these nano inclusions is dependent on several factors like feedstock modification methods, feedstock type, quality, size, shape and distribution and LPBF printing parameters [27,49].

Several researchers have studied the pitting corrosion resistance of LPBF-316L [15,27,65–67], but only a few investigated the pitting corrosion resistance of LPBF-316L with additives like CrN [27], Ag [40], CNT [42], W [39], SiC [68], CeO_2 [44], $La(NO_3).6H_2O$ [44] and soda-lime-silica [69]. Often deteriorated pitting corrosion resistance was reported with additive addition [40,44,68,69]. For example, incorporating additives like Ag, CeO_2, SiC, and $La(NO_3).6H_2O$ did not distribute well into the 316L matrix resulting in secondary phases [40,44,68]. The galvanic interaction between the formed secondary phases and the 316L matrix caused the early breakdown and poor corrosion resistance of LPBF-316L with additives. Moreover, adding soda-lime-silica has reduced the Cr in the matrix by forming a high density of Cr-Si oxide particles. This ultimately resulted in poor passivation and a faster corrosion rate, eventually declining corrosion resistance.

However, a few researchers observed enhanced pitting corrosion resistance with CrN [27] and W [39] additives.

Researchers have focused on carbon-based nanostructured materials like carbon nanotubes (CNT), nanodiamonds (ND), and graphene nanoplatelets (GNP) for decades. Researchers [41–43] reported significantly enhanced mechanical properties like tensile properties, wear resistance, and hardness of LPBF-316L with carbon-based nanostructured material addition. The improved mechanical properties were attributed to the redistribution of carbon-based nanostructured materials inside the melt pool, causing significant grain refinement in the alloy [41]. Such microstructural alterations can also help improve corrosion resistance [3,70]. Nieto et al. [42] reported retained pitting corrosion performance of LPBF-316L with CNT tested at room temperature in 0.6 M NaCl. The authors could not comment on the influence of CNT on improved or deteriorating corrosion resistance when corrosion was tested at room temperature following the polarization tests. Therefore, a detailed investigation to determine the influence of CNT on the corrosion resistance of LPBF-316L is still pending. Yin et al. [41] showed dendritic structure formation in the LPBF-316L microstructure with 1 and 5 wt.% CNT addition. This indicates an increase in the dislocation density compared to the cellular structures observed in LPBF-316L without CNT. Further, the authors have observed 100 nm long CNT in the LPBF-316L matrix. Nevertheless, the influence of these microstructural alterations on corrosion is not studied. Moreover, the presence of oxide nano inclusions and solute segregations alterations caused by CNT addition are reported in the literature. However, the influence of size and chemical composition of oxide inclusions and solute segregations on corrosion has not been investigated in the literature. Therefore, a detailed altered microstructural investigation and its influence on corrosion resistance in CNT-modified 316L is still pending. This research expands the understanding of the influence of CNTs on microstructure and their impact on retaining/improving the corrosion resistance of LPBF-316L.

In the current study, the modified feedstock was produced by ball-milling commercial 316L stainless steel powder with 1 Vol% and 2 Vol% of carbon nanotubes (CNT). The pitting corrosion resistance of LPBF-316L with 1 Vol% and 2 Vol% CNT (LPBF-316L/CNT-1 and LPBF-316L/CNT-2) is investigated in 0.6 M NaCl at room temperature, 35 ℃, and 50 ℃. This research contributes to understanding new additives and their impact on microstructure and exploring new additives to improve the corrosion resistance of LPBF-316L.

2 Experimental

2.1 Feedstock preparation and Laser powder bed fusion

The conventionally hot rolled 316L stainless steel was purchased from McMaster Carr and termed Wrought-316L. The commercial 316L stainless steel feedstock powders were procured from the EOS company. The feedstock modification was carried out by ball milling 316L feedstock powders with 1 vol% CNT and 2 vol% CNT. The laser powder bed fusion (LPBF) process was performed using an EOS M100 metal 3D printer that utilizes a 200 W ytterbium fiber laser in an argon environment. The ball milling and LPBF parameters are given in Supplementary Table 1, and Supplementary Table 2, and a detailed explanation was provided in previous literature [42]. The LPBF specimen printed using commercial feedstock is termed LPBF-316L, and composite feedstock with 1 vol% CNT and 2 vol% CNT are termed LPBF-316L/CNT-1 and LPBF-316L/CNT-2, respectively.

2.2 Characterization

The density of the LPBF specimens was calculated following Archimedes' method using Sartorius Quintix65-1S with the YDK03 density kit attached, having an accuracy of ±0.001 g/cm^3. The samples surface was prepared to 1200 grit grinding and sonicated with ethanol for 5 min. Later, an average of five readings were taken for each sample. The chemical composition of LPBF specimens was determined using an Agilent inductively coupled plasma optical emission spectrometer (ICP-OES), LECO carbon/sulfur analyzer, and LECO ONH836 oxygen/nitrogen/hydrogen analyzer following the AL0025 and ASTM E1019 standard procedures [71]. X-ray diffraction (XRD) of LPBF specimens using Rigaku smartlab X-ray diffractometer with graphite monochromatized Cu-Kα radiation (λ= 0.154056 nm). Scanning electron microscopy (SEM) using FEI Verios 460L field emission electron microscope was executed for microstructural characterization. The LPBF specimens were ground to 1200-grid SiC sandpaper and later fine polished to 0.05 µm. After polishing, the etched microstructures were revealed, followed by electro-etching with 10% oxalic acid at 15 V for 60 s (as per the ASTM A262 practice- A) [72].

Scanning/transmission electron microscopy (S/TEM) was performed using Talos F200X G2 scanning transmission electron microscope operating at 200 kV. The STEM High-angle annular dark-field (HAADF), bright-field (BF), DF 2, and DF 4 imaging of LPBF-316L and LPBF-316L/CNT-2 TEM lamellae were conducted along with SuperX energy-dispersive x-ray

spectroscopy (Super-X EDS) recorded. The Focused Ion Beam (FIB) Lift Out technique was used for S/TEM sample preparation. The electropolished samples were loaded into the Quanta 3D FEG Focused Ion Beam microscope to prepare site-specific TEM lamellae LPBF specimens. The Quanta FIB is a dual-beam instrument combining electron and ion beams for simultaneous imaging and milling. The specimens were aligned according to the interesting feature; a ~2 µm platinum cap was later deposited on the surface to protect it from ion beam damage during high-current ion beam milling. After the cross-sections were ~ 2 µm thick, they were cut and placed on TEM grids using the Omniprobe micromanipulator, enabling in-situ TEM sample preparation. The cross-section thinning and polishing were completed using low current and voltage to avoid sample amorphization and damage, and then electron transparent TEM specimens were taken for TEM characterization.

2.3 Electrochemical testing

Cyclic potentiodynamic polarization (CPP) of the LPBF-316L, LPBF-316L/CNT-1, and LPBF-316L/CNT-2 were conducted in 0.6 M or 3.5 wt.% NaCl electrolyte at room temperature, 35 ℃ and 50 ℃ on the specimens metallographically prepared to 1200-grit SiC grinding. A three-electrode flat cell with a saturated calomel reference electrode (SCE) and a platinum mesh counter electrode (CE) was used for corrosion testing. The CPP tests were initiated at 0.20 V_{SCE} below open circuit potential (OCP), and a scan rate of 1mV/s was used. The forward scan was terminated, and a reverse scan was initiated when either 1.5 V_{SCE} potential or 100 µA/cm^2 current density was reached. Before polarization, open circuit potentials were recorded while the specimens were stabilized in the test electrolyte for 1 hour. The breakdown potential (E_b) and repassivation potential (E_{rep}) were determined from the CPP curves, which were determined to compare the corrosion performance of the tested specimens.

Potentiodynamic polarization (PDP) was conducted on LPBF-316L, LPBF-316L/CNT-1, and LPBF-316L/CNT-2 specimens, and later the post-corrosion investigation was performed on the tested specimens using FEI Verios 460L field emission scanning electron microscope. The PDP test was conducted similarly to the CPP test, except the forward scan ceased when the potential reached 1.5 V_{SCE} or a current density reached 1000 µA/cm^2, and no reverse scan was initiated.

The ferric chloride ($FeCl_3$) corrosion test was conducted following the syringe droplet test, as presented in Supplementary Figure 1. Wrought-316L and LPBF specimens were 1200-ground before exposing them to 20 ml of 6 % $FeCl_3$ solution for 2 hours using the syringe. Later optical microscopy and surface profilometry were performed using Keyence VKx1100 confocal laser scanning microscope on the $FeCl_3$ corrosion-tested specimens.

Table 1 Chemical composition of unsensitized wrought and LPBF specimen in wt.%

Specimen	**O**	**Cr**	**Ni**	**Mo**	**Mn**	**Si**	**Cu**	**P**	**S**	**C**	**N**	**Fe**
EOS 316L powder		18.00	13.57	2.66	1.54	0.26	0.01	0.012	<0.005	0.005	0.07	Bal
LPBF-316L	0.069	17.24	13.58	2.79	1.38	0.280	0.007	0.019	0.010	0.012	0.068	Bal
LPBF-316L/CNT-1	0.039	17.62	13.81	2.80	1.39	0.268	0.007	0.013	0.010	0.25	0.067	Bal
LPBF-316L/CNT-2	0.027	17.12	13.51	2.77	1.36	0.269	0.005	0.017	0.011	0.48	0.067	Bal

3 Results

3.1 Density, chemical composition, and phase identification of LPBF specimen

The theoretical density of conventionally manufactured Wrought-316L is 7.93 g/cm^3. The densities (in g/cm^3) of LPBF-316L, LPBF-316L/CNT-1, and LPBF-316L/CNT-2 calculated following Archimedes' principle are 7.88, 7.81, and 7.86, respectively. The relative densities % of LPBF-316L, LPBF-316L/CNT-1, and LPBF-316L/CNT-2 are 99.3, 98.4 and 99.1 which is very close to the Wrought-316L. This shows that the densities of LPBF specimen are in an acceptable range. Table 1 presents the chemical composition (wt.%) of EOS 316L feedstock powder, LPBF-316L, LPBF-316L/CNT-1 and LPBF-316L/CNT-2. During the LPBF process, the powder bed experiences ~2000-3727 °C temperature, and the solidification rates are ~10^4-10^8 K/s [11–13]. The LPBF specimen exhibited a small reduction in chromium percentage which could be caused by evaporation of chromium during melting at extreme temperatures. The LPBF specimen with CNT addition has shown increased carbon percentage, as presented in Table 1.

The X-ray diffraction profiles of As-printed and 1200 ground LPBF-316L, LPBF-316L/CNT-1, and LPBF-316L/CNT-2 specimens are presented in Figure 1, respectively. The

LPBF-316L specimen with and without CNT exhibited a single γ-austenitic phase in both the As-printed and ground conditions.

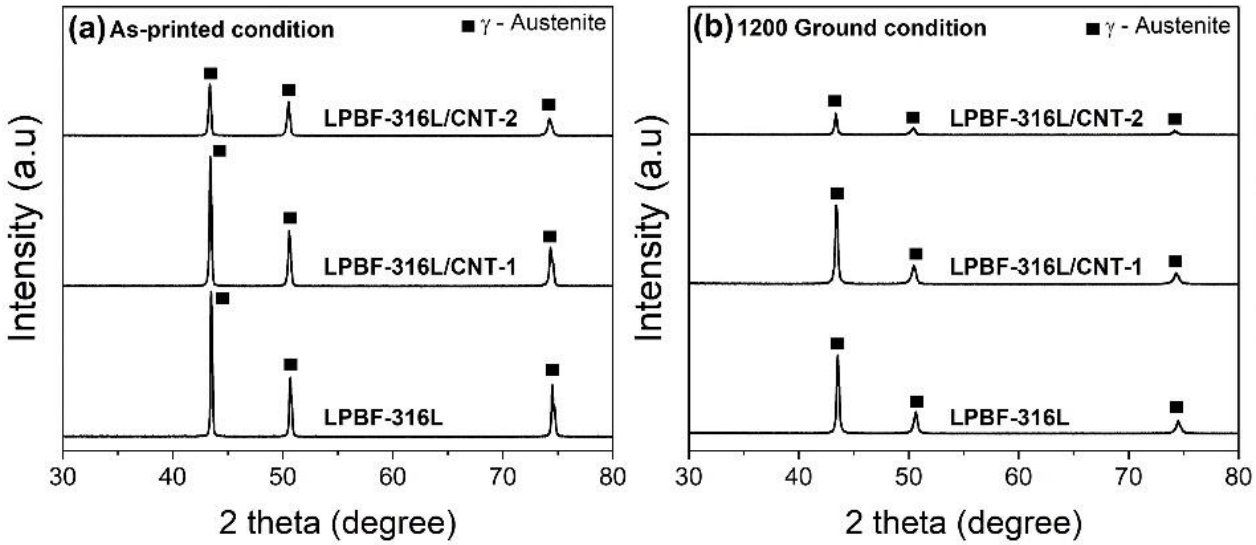

Figure 1. X-ray diffraction profiles of LPBF-316L, LPBF-316L/CNT-1, and LPBF-316L/CNT-2 (a) As-printed and (b) Ground

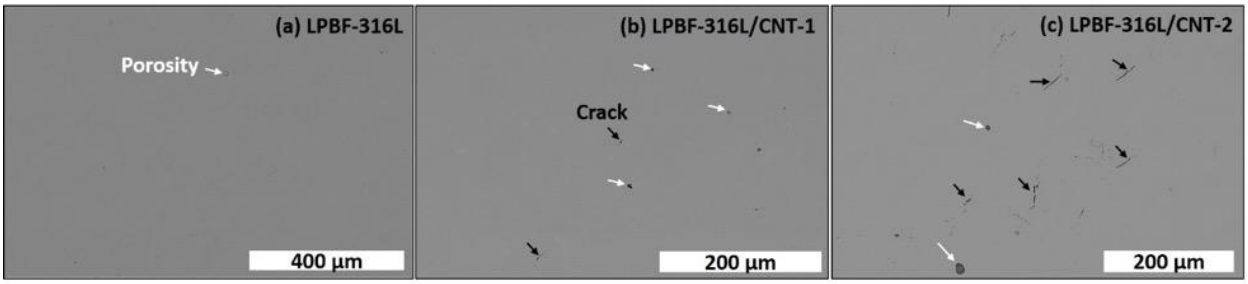

Figure 2. Backscattered electron images of (a) LPBF-316L, (b) LPBF-316L/CNT-1, and (c) LPBF-316L/CNT-2. The white and black arrows indicate manufacturing defects like porosity and micro-cracks.

3.2 Microstructure of LPBF specimens

Low magnification backscattered electron images of LPBF-316L, LPBF-316L/CNT-1, and LPBF-316L/CNT-2 specimens are presented in Figure 2(a-c), respectively. A few manufacturing defects, like porosity, were observed in all the LPBF-316L specimens. The increase in the CNT% has increased the number of pores. The addition of CNT might have significantly increased the residual

stresses due to the complex thermal history of melting and cooling cycles [42]. This resulted in higher brittleness, and several cracks have been observed in LPBF specimens with CNT [42].

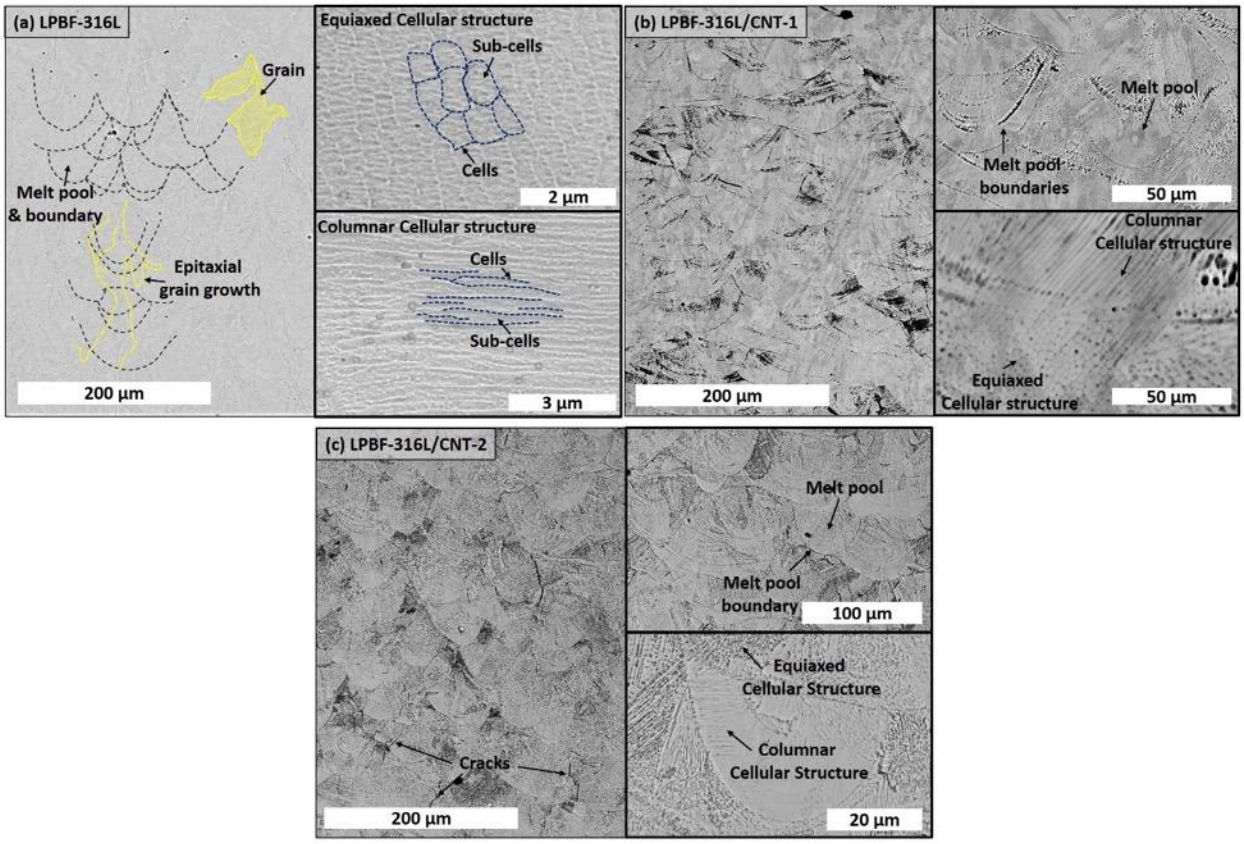

Figure 3. Backscattered electron images of etched microstructure of (a) LPBF-316L, (b) LPBF-316L/CNT-1, and (c) LPBF-316L/CNT-2. The black dotted lines indicate the melt pool boundaries, whereas the yellow lines indicate the grain boundaries. The blue dotted lines highlight the cell boundaries.

The etched micrographs of LPBF-316L, LPBF-316L/CNT-1, and LPBF-316L/CNT-2 are presented in Figure 3(a-c), respectively. Overlapped melt pools and melt pool boundaries have been observed in all the specimens indicating that sufficient melting has occurred and dense component is printed. The CNT addition did not influence the melt pool dimensions. The melt pool boundaries did not impact grain growth phenomena, particularly at the center of the melt pool, where grains hold the geometric and crystallographic orientation, as evidenced by the epitaxial grain growth [60,73]. This epitaxial growth occurs when a new grain growing direction aligns with the seed crystal in the underlying layer, nearest to the melt pool's thermal gradient [73]. Such epitaxial growth has been observed in all the LPBF specimens, Figure 3. The melt pool boundaries, particularly the interface boundaries between two pools, had a comparatively high corrosion rate

in the CNT-added LPBF specimen, as shown in Figure 3(b and c), respectively. The commonly known cellular structures, which can be viewed as equiaxed and columnar cellular structures, are observed in all the LPBF specimens [27,28,74]. The addition of CNT has increased the solidification rates, resulting in the formation of short secondary dendritic arms on the side of the columnar cellular structure, as seen in Figure 3(c), which was also observed by Yin et al. [41] in LPBF-316L specimen with 1 wt.% CNT. Inside each cell of either equiaxed or columnar cellular structure, fine cells were observed at the lower accelerating voltage and termed sub-cells [3,27,44], as depicted in Figure 3a. The CNT specimens showed aggressive corrosion when subjected to electro-etching and hence challenging to see sub-cells using scanning electron microscopy in CNT-added specimens. However, the transmission electron microscopy revealed the presence of sub-cells in 1 and 2 vol% CNT specimens (Figure 4).

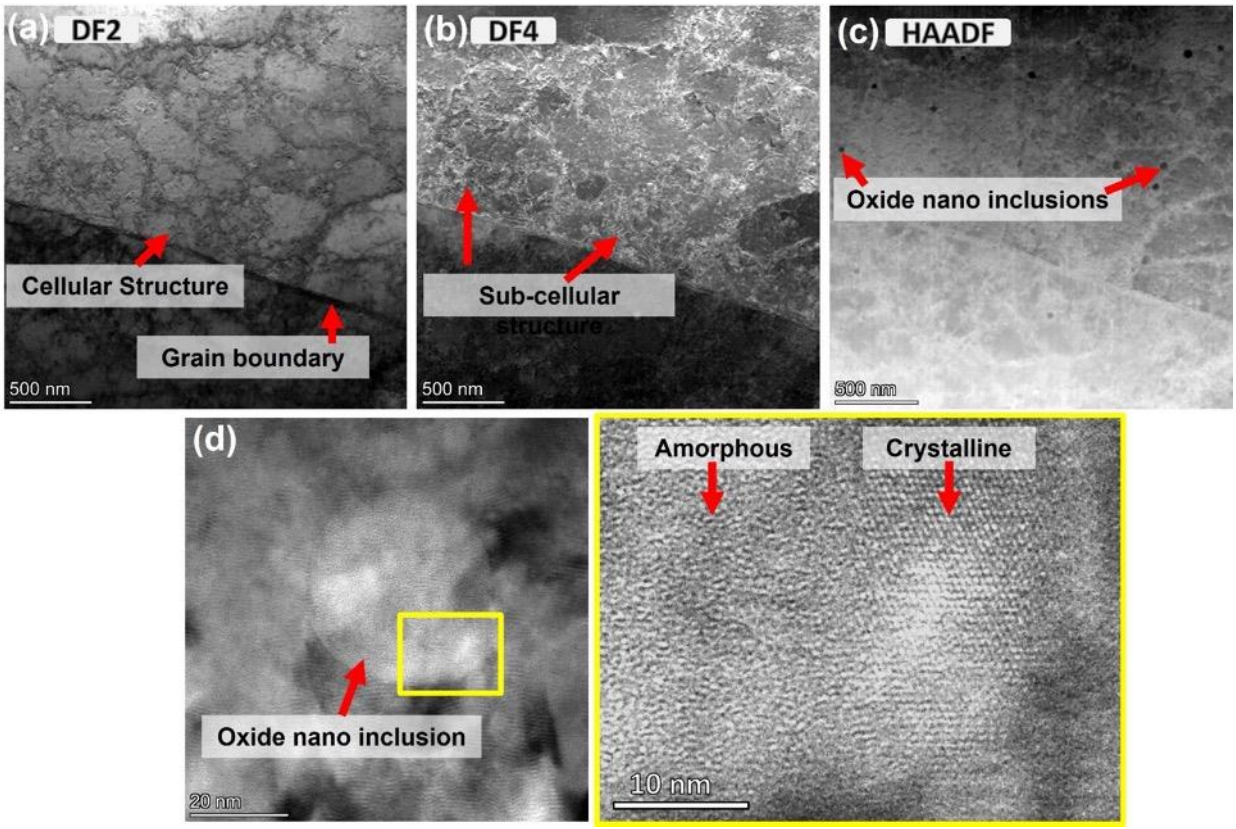

Figure 4. S/TEM micrographs depicting the cellular structure,sub-cellular structure, and nano oxide inclusions of LPBF-316L. The red arrows point out the respective structural features mentioned in the image. The yellow square is a high-magnification image of part of the oxide nano inclusion shown in (d).

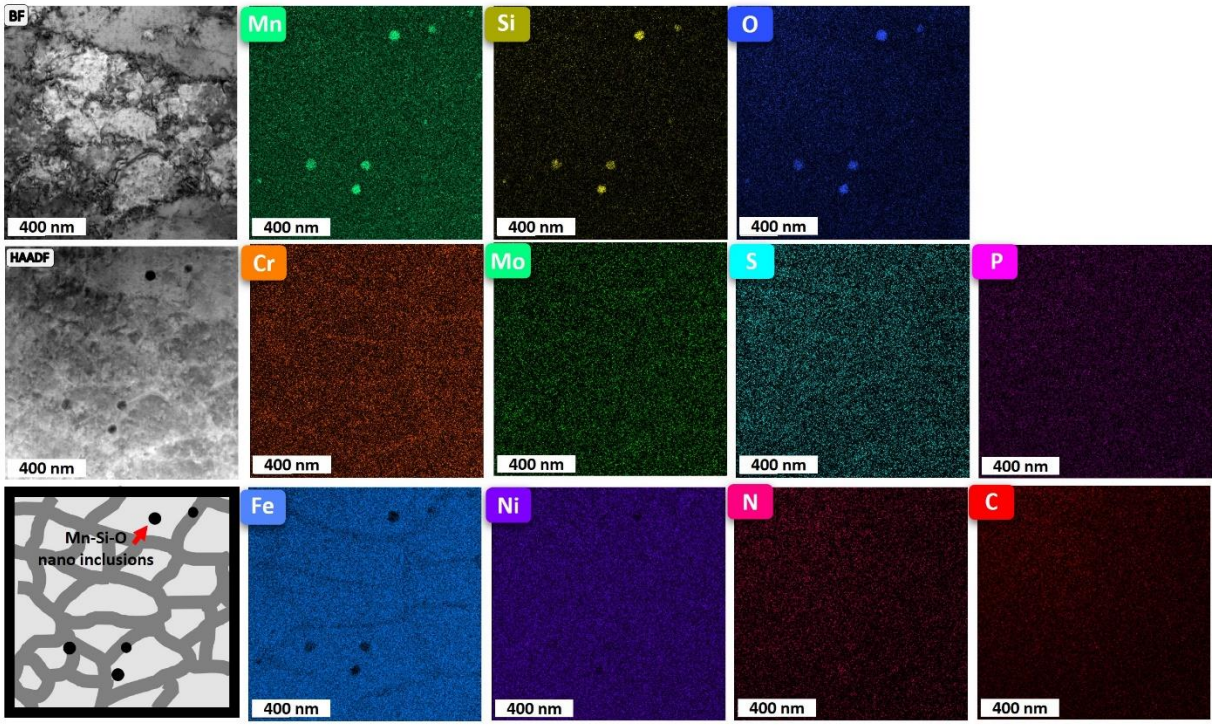

Figure 5. STEM-EDS micrographs of LPBF-316L revealing the solute segregation along the cellular boundaries and the presence of Mn-Si-O oxide nano inclusions.

The S/TEM micrographs of LPBF-316L are presented in Figure 4. The cellular and sub-cellular structures were revealed using DF2 and DF4 micrographs, as shown in Figure 4(a and c), respectively. A dense entangled dislocation network was observed along the cellular boundaries, and a thin entangled dislocation network was observed along sub-cellular boundaries, as depicted in the DF4 micrograph of Figure 4c. The dark circles in HAADF micrograph are the oxide nano inclusions in LPBF-316L (Figure 4b). These oxide nano inclusions were observed majorly along the cellular boundaries and a few inside the cell. The oxide nano inclusions are partially amorphous and crystalline, as revealed by Figure 4d, unlike few studies [22,26] where only amorphous nature was reported. The diameter of oxide nano inclusions in LPBF-316L is 44 ± 12 nm. The STEM-EDS elemental maps of cellular structure revealing the composition of oxide nano inclusions and solute segregation are presented in Figure 5. The oxide nano inclusions comprised Mn, Si, and O. Along the cellular boundaries, solute segregation of Cr, Mo, and S and depletion of Fe and Ni were observed (Figure 5).

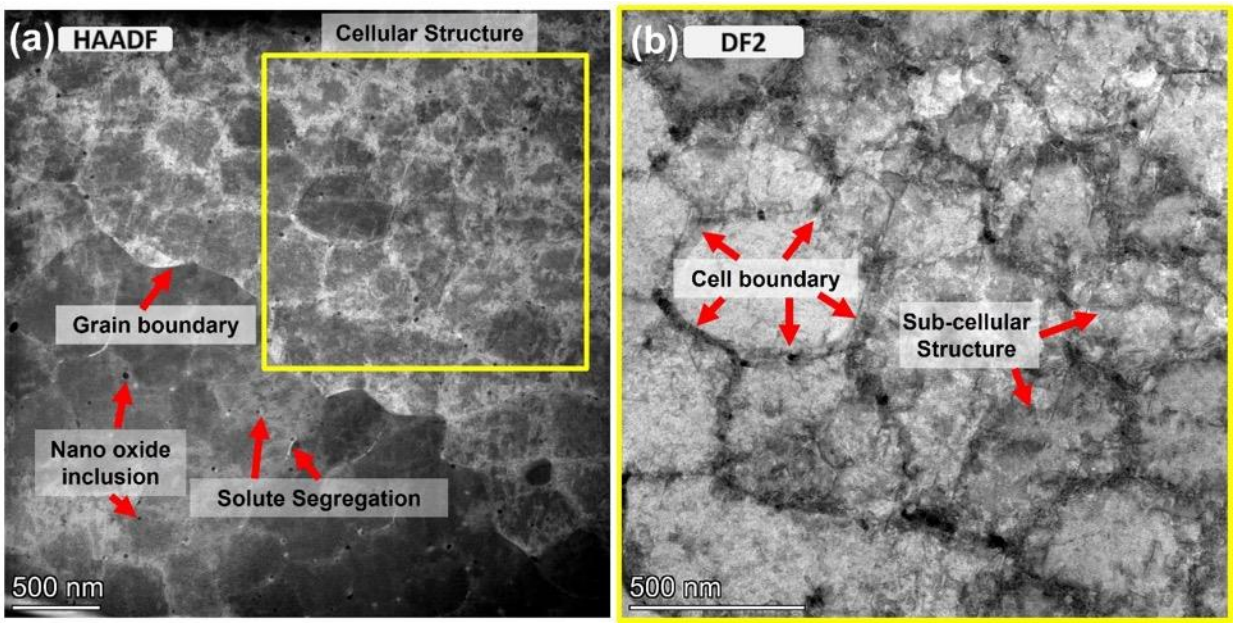

Figure 6. S/TEM micrographs showing the cellular structure,sub-cellular structure, and nano oxide inclusions of LPBF-316L/CNT-2. The red arrows point out the respective structural features mentioned in the image. The yellow square is a high-magnification image of the cellular structure shown in (a).

The S/TEM micrographs of LPBF-316L/CNT-2 are depicted in Figure 6. The cellular and sub-cellular structures with cells, cell boundaries, sub-cells, and sub-cell boundaries are revealed using HAADF and DF2 micrographs, as presented in Figure 6(a-b). The cellular and sub-cellular boundaries have dense and thin entangled dislocation networks in LPBF-316L/CNT-2, similar to LPBF-316L. A high density of oxide nano inclusions with a 15 ± 7 nm diameter was observed along the cellular boundaries and within the cells in LPBF-316L/CNT-2, as shown in Figure 6a. Low and high magnification S/TEM-EDS elements maps across the cellular structure of LPBF-316L/CNT-2 are presented in Figure 7. The cellular boundaries in LPBF-316L/CNT-2 were seen to have solute segregation of Cr, Mo, S, P, O, and C, and particularly at the triple point junctions of cellular boundaries, enriched solute segregation of the same elements was observed. Along with the solute segregation, the cellular boundaries have a depletion of Fe and Ni in LPBF-316L/CNT-2, similar to LPBF-316L. Moreover, the carbon from CNT or 316L feedstock was observed segregating near very few regions of cellular boundaries and cells, as pointed out in Figure 7(a-b), respectively, using the red arrow. The oxide nano inclusions consisted of Mn, Si, and O in LPBF-316L/CNT-2, similar to LPBF-316L, as shown in Figure 7a. This indicates that CNT addition did

not influence the composition of the oxide nano inclusions. The majority of the oxide nano inclusions were detected at the triple point junctions of the cellular boundaries where enriched solute segregation was seen. Also, a few nano inclusions were observed along the cellular boundaries and inside the cells, as shown in Figure 7b. It is worth noting that the CNT addition has caused significant refinement in the oxide nano inclusion size and altered the elemental solute segregation across the cellular boundaries.

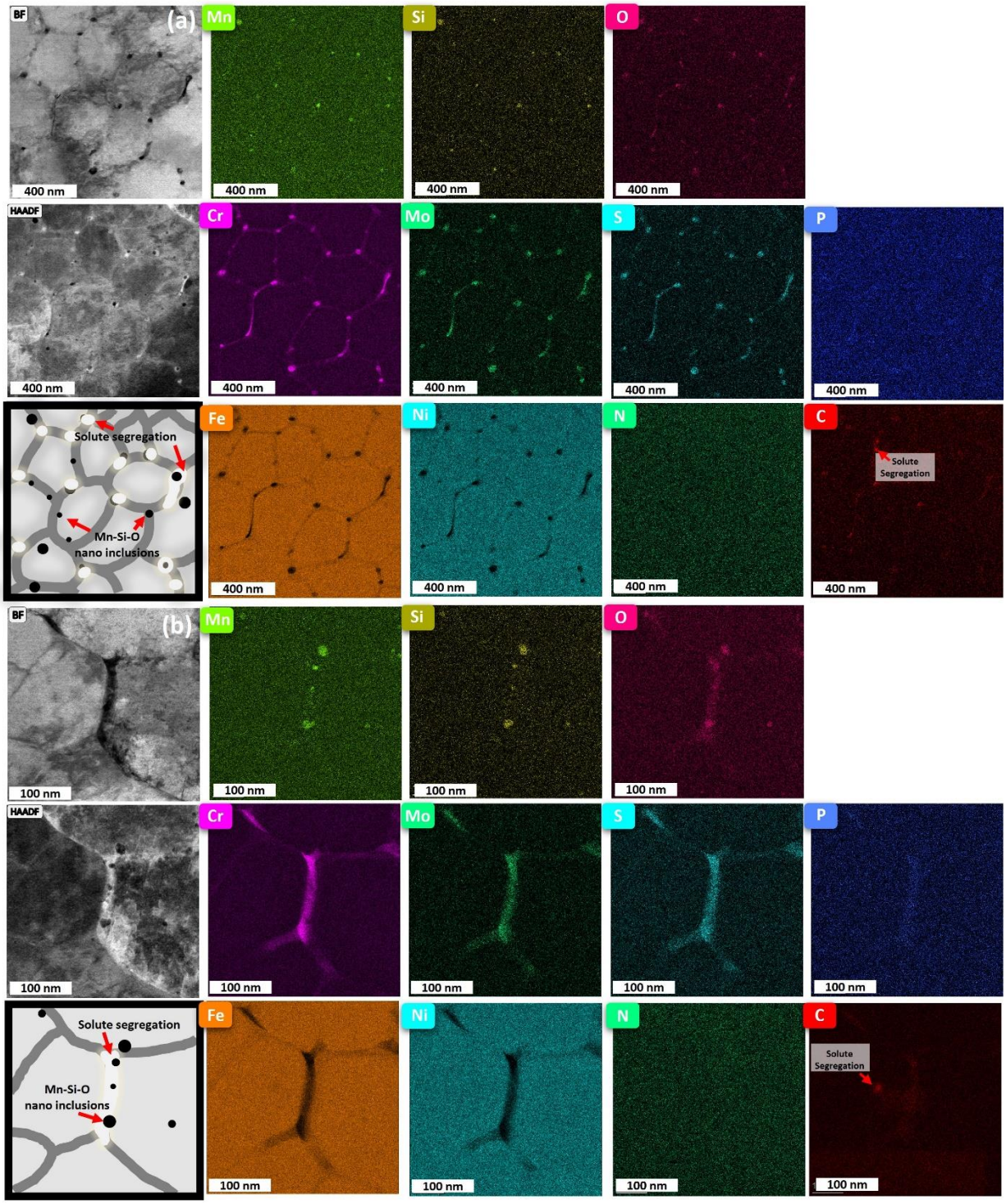

Figure 7. Low and high magnification STEM-EDS micrographs of LPBF-316L/CNT-2 in (a) low and (b) high magnifications. The black circles represent the Mn-Si-O nano inclusions, and the bring white region represents the solute segregation along the cellular boundaries in the schematics. The red arrows point out the respective structural features in the schematic.

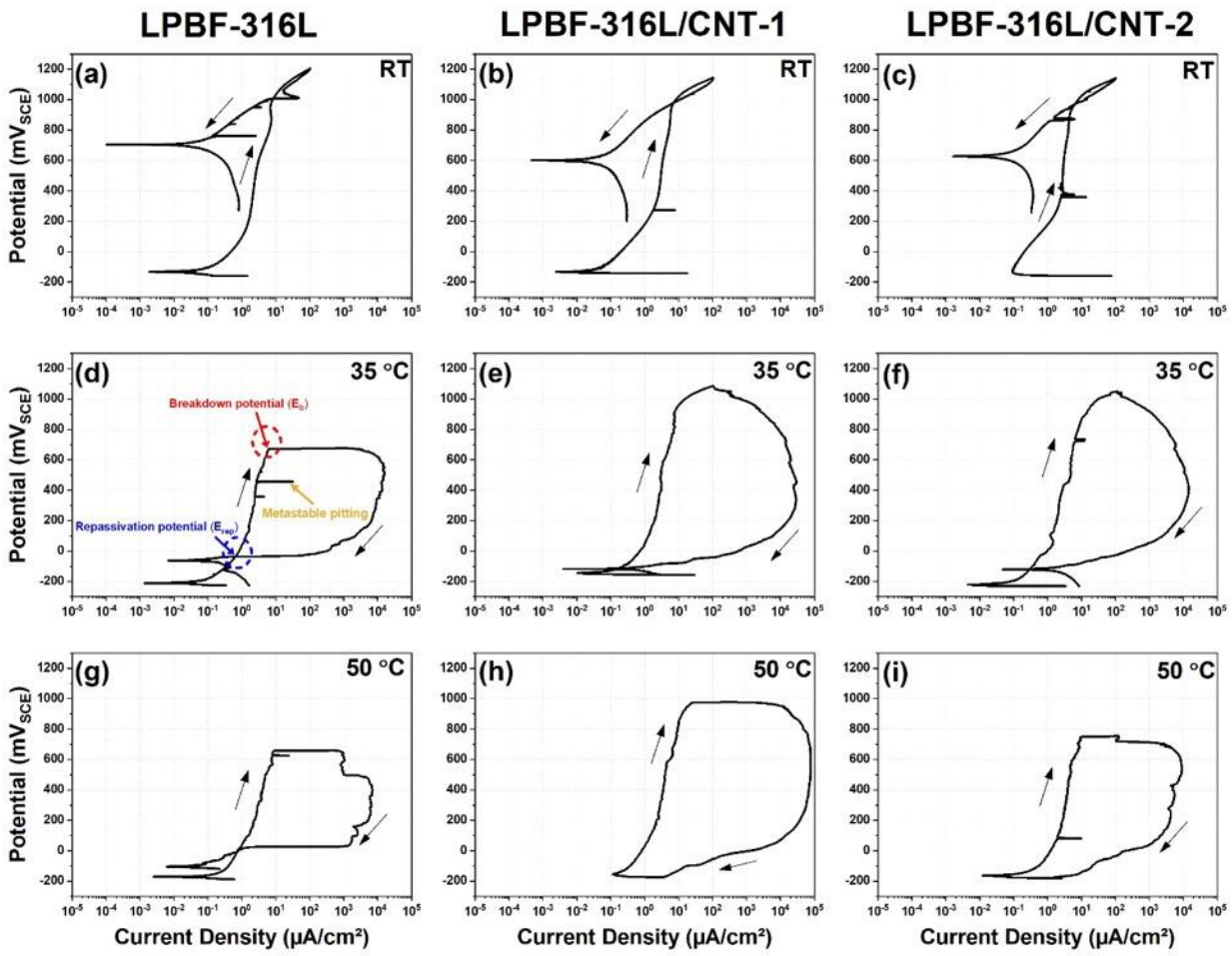

Figure 8. Cyclic potentiodynamic polarization (CPP) of (a) LPBF-316L, (b) LPBF-316L/CNT-1, and (c) LPBF-316L/CNT-2 tested in 0.6 M NaCl at room temperature (RT), 35 ℃ and 50 ℃ temperature. The black arrows represent the scan direction of CPP curves. The red, blue, and yellow arrows represent the breakdown, repassivation potentials, and Metastable pitting regions, respectively.

3.3 Corrosion performance of LPBF specimens

The pitting corrosion resistance evaluated by the cyclic potentiodynamic polarization (CPP) curves of LPBF-316L, LPBF-316L/CNT-1, and LPBF-316L/CNT-2 specimens tested in 0.6 M NaCl at room temperature (RT), 35 ℃ and 50 ℃ temperatures are presented in Figure 8. The breakdown potential (E_b) and repassivation potential (E_{rep}) determined from the CPP graphs are presented in Figure 9. The corrosion performance of LPBF-316L, LPBF-316L/CNT-1, and LPBF-316L/CNT-2 tested at RT and in 0.6 M NaCl was observed to be similar as evidence by similar E_b and E_{rep}, Figure 8(a-c) and Figure 9. The LPBF-316L, LPBF-316L/CNT-1, and LPBF-316L/CNT-2 exhibited E_b of 987 ± 31 mV_{SCE}, 934 ± 21 mV_{SCE}, and 912 ± 17 mV_{SCE}, respectively, and E_{rep} of 1041 ± 68 mV_{SCE}, 970 ± 3 mV_{SCE}, and 974 ± 3 mV_{SCE}, respectively. The CPP tests conducted at RT were insufficient to judge the corrosion resistance of LPBF specimens with and without CNT addition due to similar breakdown and repassivation potentials [42], Figure 9. Hence, the CPP testing temperature was increased to 35 ℃ and 50 ℃ to evaluate the same.

The CPP tests of LPBF-316L, LPBF-316L/CNT-1, and LPBF-316L/CNT-2 conducted at 35 ℃ are presented in Figure 8(d-f), respectively. During the forward scan, the LPBF-316L specimen exhibited metastable pitting, followed by a passive film breakdown, as shown in Figure 8d. The LPBF-316L specimen exhibited E_b of 630 ± 61 mV_{SCE} during the forward scan. The reverse scan was commenced after reaching 100 $\mu A/cm^{2,}$ and E_{rep} of 47 ± 98 mV_{SCE} was observed. The LPBF-316L/CNT-1 and LPBF-316L/CNT-2 specimen exhibited no or minor metastable pitting compared to the LPBF-316L specimen, and E_b of 913 ± 77 mV_{SCE} and 924 ± 60 mV_{SCE} was observed during the forward scan (Figure 8(e-f) and Figure 9). During the reverse scan, E_{rep} of -65 ± 48 mV_{SCE} and -132 ± 18 mV_{SCE} was seen in LPBF-316L/CNT-1 and LPBF-316L/CNT-2 specimens, respectively (Figure 8(e-f) and Figure 9).

The CPP tests of LPBF-316L, LPBF-316L/CNT-1, and LPBF-316L/CNT-2 conducted at 50℃ are presented in Figure 8(g-i), respectively. The LPBF-316L, LPBF-316L/CNT-1, and LPBF-316L/CNT-2 exhibited E_b of 552 ± 164 mV_{SCE}, 892 ± 98 mV_{SCE}, and 554 ± 117 mV_{SCE}, respectively (Figure 8(g-i) and Figure 9). The E_{rep} of LPBF-316L was -46 ± 58 $mV_{SCE,}$ whereas LPBF-316L/CNT-1 and LPBF-316L/CNT-2 did not repassivate (Figure 8(h-i) and Figure 9). The slightly reduced corrosion resistance of LPBF-316L/CNT-2 compared to LPBF-316L/CNT-1 could be due to the high number of manufacturing defects like pores and cracks.

Overall, the LPBF-316L, LPBF-316L/CNT-1, and LPBF-316L/CNT-2 specimens showed decreasing breakdown potentials and repassivation potentials with the increase in the CPP testing temperature (Figure 9), and such phenomenon was also observed for 316L stainless in literature [75,76]. The breakdown potential of LPBF-316L with CNT addition was enhanced, as evidenced by CPP at 35 ℃ and 50 ℃ CPP testing temperatures. The LPBF-316L/CNT-1 and LPBF-316L/CNT-2 did not exhibit repassivation potentials at 50℃ CPP testing, which could be due to high crevice corrosion or intense corrosion across the manufacturing defects like porosity and crack. To investigate that, post-corrosion characterization was performed after potentiodynamic polarization (PDP) tests conducted at RT, 35 ℃, and 50 ℃ temperatures.

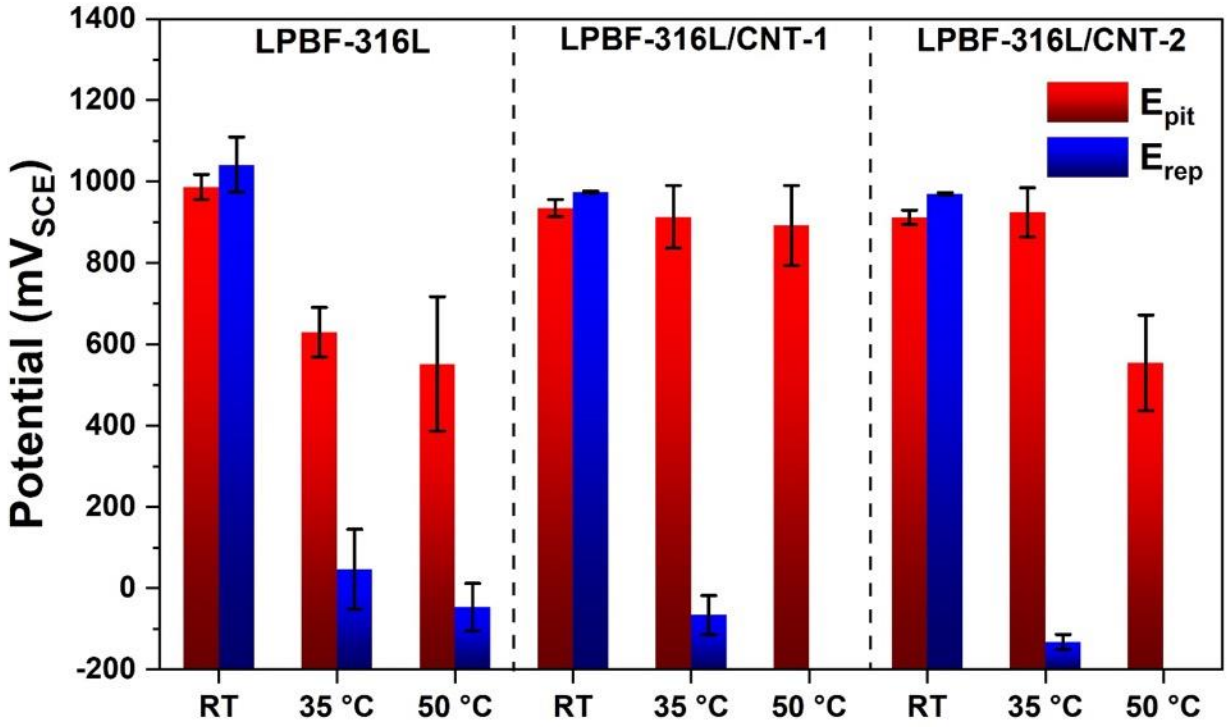

Figure 9. Corrosion performance comparison between LPBF-316L, LPBF-316L/CNT-1, and LPBF-316L/CNT-2 tested in 0.6 M NaCl at room temperature (RT), 35 ℃, and 50 ℃ temperature.

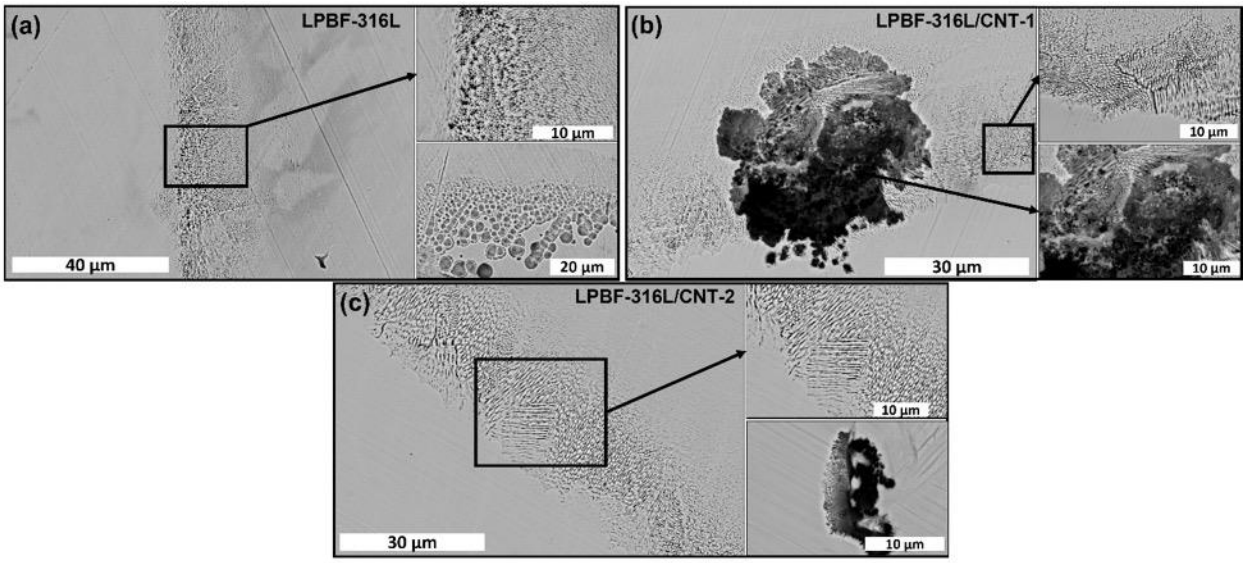

Figure 10. Post-corrosion characterization after potentiodynamic polarization of (a) LPBF-316L, (c) LPBF-316L/CNT-1 and (c) LPBF-316L/CNT-2 conducted at room temperature

3.4 Post-corrosion characterization

3.4.1 After pitting corrosion of LPBF specimens

The post-corrosion characteristics of LPBF-316L, LPBF-316L/CNT-1, and LPBF-316L/CNT-2 after performing potentiodynamic polarization (PDP) tests conducted at room temperature were presented in Figure 10. The LPBF-316L, LPBF-316L/CNT-1, and LPBF-316L/CNT-2 specimens PDP tested at RT did not exhibit pit yet, and only minor crevice corrosion was observed at the periphery of the exposed area to the electrolyte, as shown in Figure 10(a-c). This minor crevice corrosion has exhibited corroded cellular boundaries and intact cells like intercellular corrosion [27]. The LPBF-316L/CNT-1 and LPBF-316L/CNT-2 showed aggressive corrosion at the manufacturing defects like porosity and cracks, as exhibited in Figure 10(b and c), respectively. Figure 10c exposes the short secondary dendritic arms along the sides of the columnar cellular structure revealed by the crevice corrosion.

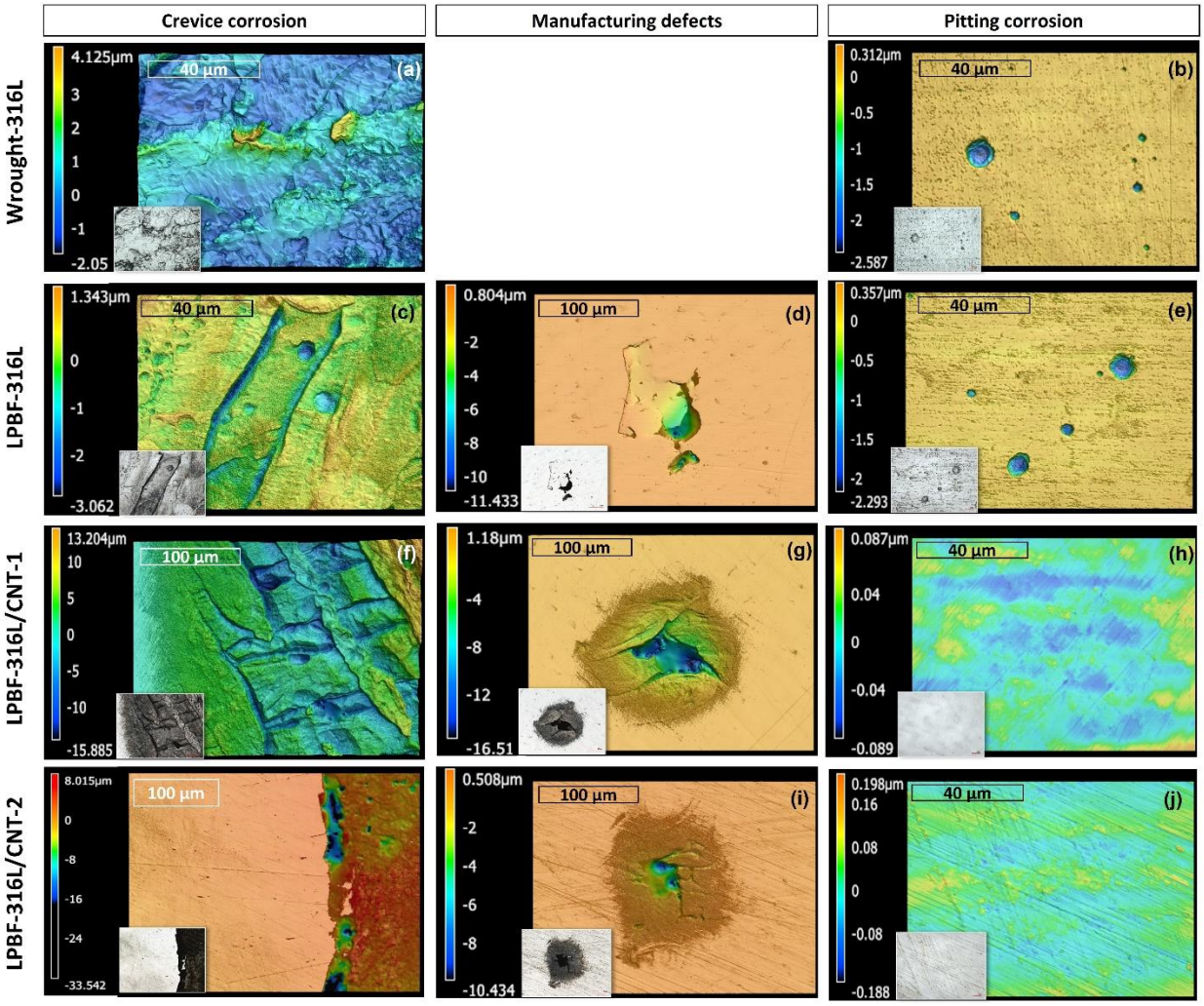

Figure 11. Surface profilometry images of (a-b) Wrought-316L, (c-e) LPBF-316L, (f-h) LPBF-316L/CNT-1 and (i-j) LPBF-316L/CNT-2 after 2 hours of 6% $FeCl_3$ syringe droplet test

3.4.2 After 2 hours of immersion of LPBF specimens in 6 % $FeCl_3$

Surface profilometry images of Wrought-316L, LPBF-316L, LPBF-316L/CNT-1, and LPBF-316L/CNT-2 after 2 hours of 6% $FeCl_3$ syringe droplet test are presented in Figure 11. Wrought-316L, LPBF-316L, LPBF-316L/CNT-1, and LPBF-316L/CNT-2 specimens showed crevice corrosion after 2 hours of exposure to 6% $FeCl_3$. The wrought-316L specimen exhibited step-by-step deterioration of grains in crevice corrosion, as shown in Figure 11(a). The LPBF-316L and LPBF-316L specimens with CNT exhibited aggressively corroded melt pool boundaries, as presented in Figure 11(c and f), respectively. The manufacturing defects like lack-of-fusion pores and microcracks in LPBF-316L, LPBF-316L/CNT-1, and LPBF-316L/CNT-2, were highly corroded after 2 hours of exposure to 6% $FeCl_3$, as depicted in Figure 11(d,g, and i), respectively.

Wrought-316L and LPBF-316L specimens showed a high density of pits indicating pitting corrosion, Figure 11(b and e), respectively, whereas LPBF-316L/CNT-1 and LPBF-316L/CNT-2 did not reveal any visible pits, as presented in Figure 11(h and j), respectively, after 2 hours of exposure to 6% $FeCl_3$. Overall, the pitting corrosion resistance of LPBF-316L improved due to CNT addition.

4 Discussion

Often the corrosion resistance of conventionally 316L stainless steel is determined by (1) secondary phase particles or inclusions composition, (2) size of the inclusions, and (3) chromium deletion around the inclusions. The corrosion performance of LPBF-316L has been extensively correlated with the inclusion present in the microstructure [3,44,55,65]. Researchers [56,57,77] have reported that three types of inclusions can initiate corrosion in austenitic stainless steel: 1. Manganese sulphide (MnS) 2. Multielement oxides of Al, Mn, Cr, Ti, V, etc. 3. Mixtures of oxide and sulphide inclusions. In conventionally manufactured 316L, the MnS inclusions act as potential cathodic particles and cause corrosion initiation in an anodic γ-austenitic steel matrix [55]. The chromium absence in the MnS inclusion causes a local disturbance in the passive film formation, and this defective passive region is highly susceptible to initiating corrosion. The oxidated MnS inclusion results in sulphur-containing species formation, including sulphur, sulphides, hydrosulphides, and thiosulphates [55]. Consequently, a sulphur crust is formed, again preventing the passive film growth resulting in further metal dissolution and stable pit growth. In LPBF-316L, MnS inclusions were not observed, which is also often reported in the literature [55,63,65,67]. Researchers [62,78,79] have shown the formation of Si-containing inclusions in 316L and the possibility of corrosion initiation around them. In current research, Mn-Si-O inclusions were observed in the microstructure of LPBF-316L. From this, it can be anticipated that Mn-Si-O is causing the corrosion initiation in LPBF-316L; however, the LPBF-316L/CNT-2 also showed Mn-Si-O inclusions only (Figure 5 and Figure 7). The CNT addition did not alter the elemental composition of nano inclusions, and therefore, there is no influence of inclusion composition on corrosion enhancement.

The next possible criterion for the enhanced corrosion resistance of LPBF-316L with CNT can be the size of the inclusions [56,57]. The nano inclusions of LPBF-316L and LPBF-316L/CNT-2 are 44 ± 12 nm and 15 ± 7 nm, respectively (Figure 4 and Figure 6). The MnS

inclusions of ~ 0.7 µm or above were reported to act as cathodic particles in conventionally manufactured 316L stainless steel [56,57]. To the best of the authors' knowledge, the effect of fine oxide inclusions in the nanometer range on the corrosion of stainless steel has not been reported, possibly due to their rarity in conventional stainless steels. However, the role of fine intermetallics or precipitates has been extensively studied in aluminum alloys. For example, Gupta et al. [80,81] and Ralston et al. [82,83] investigated the influence of precipitate size corrosion and concluded existence of critical precipitate size below which pitting corrosion does not initiate. Similarly, there may exist a critical size of the oxide inclusions below which the pitting corrosion may not initiate. For the LPBF 316L, the critical size may lie between ~15 and 44 nanometers. The refined nano inclusions in LPBF-316L/CNT-2 might have been below critical size and therefore incapable of causing corrosion initiation, and hence enhanced corrosion resistance is observed. Understanding the role of such find oxide inclusions on corrosion of stainless steels becomes relevant in additively manufactured stainless steel and further research would be needed to investigate the existence of critical size and corrosion mechanisms.

Moreover, the corrosion initiation in conventionally manufactured 316L stainless steel is due to the depletion of 200 – 500 nm chromium surrounding the MnS inclusions [55]. In LPBF-316L/CNT-2, even if the refined nano inclusions caused corrosion initiation, the enriched solute segregation of Cr and O surrounding the nano inclusions might aid in controlling it and promotes the passivation kinetics by forming chromium oxide (Figure 7) and hence, the corrosion resistance might have been improved. Nonetheless, this research shows that controlling the size of nano inclusions could be a strategy to improve corrosion resistance.

Furthermore, the introduction of CNTs has induced modifications in solute segregation along cellular boundaries. Specifically, in LPBF-316L/CNT-2, there was observed elemental segregation of Cr, Mo, S, P, C, and O, whereas LPBF-316L exhibited elemental segregation of only Cr, Mo, and S. Researchers [84,85] highlighted the distinction in potential between (5-10 mV) cellular boundaries and the interior of LPBF-316L cells, attributing it to the onset of corrosion facilitated by micro-galvanic coupling. It is plausible that the altered elemental segregation in LPBF-316L/CNT-2 might have diminished the potential difference between cells and their boundaries, potentially contributing to enhanced corrosion resistance. Nonetheless, it's important to note that while the experimental data gathered in this study falls short of substantiating this assertion, it is still of significance.

Feedstock modification is a practical method for refining the size of inclusions and controlling microstructure. There could be several other additives like CNT, yet to be explored, that can aid in altering the composition and size of the oxide nano inclusions and can enhance the desired properties.

5 Conclusion

The influence of 1 and 2 vol% carbon nanotubes (CNT) on microstructure and corrosion performance of laser powder bed fusion (LPBF) printed 316L was investigated. The CNT addition caused microstructural changes like oxide nano inclusions refinement and altered solute segregation of Cr, Mo, S, P, C, and O along the cellular boundaries. The LPBF-316L with CNT has enhanced the breakdown potential when tested in 0.6 M NaCl at room temperature (RT), 35 ℃, and 50 ℃. Immersion in 6 wt.% % $FeCl_3$ and subsequent surface analyses revealed higher pitting corrosion resistance in samples produced using CNT modified feedstock. Electrochemical and immersion tests indicated that pitting corrosion resistance of 316L stainless steel could be enhanced by the modification of feedstock by the CNT. The enhanced corrosion resistance due to the CNT could be attributed to the refined oxide nano inclusions and segregation of chromium around the oxide nano inclusions.

6 Data availability

The raw/processed data supporting this research's findings can be shared upon reasonable request.

7 CRediT authorship contribution statement

VBV: Conceptualization, Methodology, Writing – original draft, Methodology, Data curation, Formal analysis, Visualization, and Investigation. JC: Methodology and Investigation, Writing – editing and reviewing. TN: Methodology and Investigation AN: Methodology and Investigation. RKG: Conceptualization, Methodology, Supervision, and Writing – editing and reviewing.

8 Competing interests

The authors report no declaration of interest.

9 Acknowledgment

RKG acknowledges the Office of Naval Research for funding this research under the contracts ONR: N00014-21-1-2489 with Dr. David Shifler as a program officer. The authors want to acknowledge the Analytical Instrumentation Facility (AIF) at North Carolina State University, supported by the State of North Carolina and the National Science Foundation (award number ECCS-2025064). The AIF is a member of the North Carolina Research Triangle Nanotechnology Network (RTNN), a site in the National Nanotechnology Coordinated Infrastructure (NNCI).

10 References

[1] K. Geenen, A. Röttger, W. Theisen, Corrosion behavior of 316L austenitic steel processed by selective laser melting, hot-isostatic pressing, and casting, Mater. Corros. 68 (2017) 764–775. https://doi.org/10.1002/maco.201609210.

[2] S.A.M. Tofail, E.P. Koumoulos, A. Bandyopadhyay, S. Bose, L. O'Donoghue, C. Charitidis, Additive manufacturing: scientific and technological challenges, market uptake and opportunities, Mater. Today. 21 (2018) 22–37. https://doi.org/10.1016/j.mattod.2017.07.001.

[3] V.B. Vukkum, R.K. Gupta, Review on corrosion performance of laser powder-bed fusion printed 316L stainless steel: Effect of processing parameters, manufacturing defects, post-processing, feedstock, and microstructure, Mater. Des. 221 (2022) 110874. https://doi.org/10.1016/j.matdes.2022.110874.

[4] G. Sander, J. Tan, P. Balan, O. Gharbi, D.R. Feenstra, L. Singer, S. Thomas, R.G. Kelly, J.R. Scully, N. Birbilis, Corrosion of additively manufactured alloys: A review, Corrosion. 74 (2018) 1318–1350. https://doi.org/10.5006/2926.

[5] V.B. Vukkum, T. Ray, A. Karmakar, S. Das, Microstructure–Texture–Mechanical Property Correlation in Laser-Welded Dual-Phase and Interstitial-Free Steel Blanks, J. Mater. Eng. Perform. (2023) 1–12. https://doi.org/10.1007/s11665-023-07959-6.

[6] D. Kong, C. Dong, X. Ni, X. Li, Corrosion of metallic materials fabricated by selective laser melting, Npj Mater. Degrad. 3 (2019). https://doi.org/10.1038/s41529-019-0086-1.

[7] M.J.K. Lodhi, K.M. Deen, M.C. Greenlee-Wacker, W. Haider, Additively manufactured

316L stainless steel with improved corrosion resistance and biological response for biomedical applications, Addit. Manuf. 27 (2019) 8–19. https://doi.org/10.1016/j.addma.2019.02.005.

[8] M. Atapour, X. Wang, K. Färnlund, I. Odnevall Wallinder, Y. Hedberg, Corrosion and metal release investigations of selective laser melted 316L stainless steel in a synthetic physiological fluid containing proteins and in diluted hydrochloric acid, Electrochim. Acta. 354 (2020) 136748. https://doi.org/10.1016/j.electacta.2020.136748.

[9] S. Alvi, K. Saeidi, F. Akhtar, High temperature tribology and wear of selective laser melted (SLM) 316L stainless steel, Wear. 448–449 (2020) 203228. https://doi.org/10.1016/j.wear.2020.203228.

[10] M. Song, M. Wang, X. Lou, R.B. Rebak, G.S. Was, Radiation damage and irradiation-assisted stress corrosion cracking of additively manufactured 316L stainless steels, J. Nucl. Mater. 513 (2019) 33–44. https://doi.org/10.1016/J.JNUCMAT.2018.10.044.

[11] M.J. Ansari, D.S. Nguyen, H.S. Park, Investigation of SLM process in terms of temperature distribution and melting pool size: Modeling and experimental approaches, Materials (Basel). 12 (2019). https://doi.org/10.3390/ma12081272.

[12] T. Mede, A. Kocjan, I. Paulin, M. Godec, Numerical mesoscale modelling of microstructure evolution during selective laser melting, Metals (Basel). 10 (2020) 1–15. https://doi.org/10.3390/met10060800.

[13] P.A. Hooper, Melt pool temperature and cooling rates in laser powder bed fusion, Addit. Manuf. 22 (2018) 548–559. https://doi.org/10.1016/J.ADDMA.2018.05.032.

[14] A. Eliasu, A. Czekanski, S. Boakye-Yiadom, Effect of laser powder bed fusion parameters on the microstructural evolution and hardness of 316L stainless steel, Int. J. Adv. Manuf. Technol. 113 (2021) 2651–2669. https://doi.org/10.1007/s00170-021-06818-9.

[15] G. Sander, A.P. Babu, X. Gao, D. Jiang, N. Birbilis, On the effect of build orientation and residual stress on the corrosion of 316L stainless steel prepared by selective laser melting, Corros. Sci. 179 (2021) 109149. https://doi.org/10.1016/j.corsci.2020.109149.

[16] M. Laleh, A.E. Hughes, S. Yang, J. Li, W. Xu, I. Gibson, M.Y. Tan, Two and three-dimensional characterisation of localised corrosion affected by lack-of-fusion pores in 316L stainless steel produced by selective laser melting, Corros. Sci. 165 (2020) 108394. https://doi.org/10.1016/j.corsci.2019.108394.

[17] G. Wang, Q. Liu, H. Rao, H. Liu, C. Qiu, Influence of porosity and microstructure on mechanical and corrosion properties of a selectively laser melted stainless steel, J. Alloys Compd. 831 (2020) 154815. https://doi.org/10.1016/j.jallcom.2020.154815.

[18] R. Li, Y. Shi, Z. Wang, L. Wang, J. Liu, W. Jiang, Densification behavior of gas and water atomized 316L stainless steel powder during selective laser melting, Appl. Surf. Sci. 256 (2010) 4350–4356. https://doi.org/10.1016/j.apsusc.2010.02.030.

[19] Y. Liu, Y. Yang, D. Wang, A study on the residual stress during selective laser melting (SLM) of metallic powder, Int. J. Adv. Manuf. Technol. 87 (2016) 647–656. https://doi.org/10.1007/s00170-016-8466-y.

[20] J.A. Cherry, H.M. Davies, S. Mehmood, N.P. Lavery, S.G.R. Brown, J. Sienz, Investigation into the effect of process parameters on microstructural and physical properties of 316L stainless steel parts by selective laser melting, Int. J. Adv. Manuf. Technol. 76 (2014) 869–879. https://doi.org/10.1007/s00170-014-6297-2.

[21] C.S. Witharamage, M.A. Alrizqi, J. Chirstudasjustus, A.A. Darwish, T. Ansell, A. Nieto, R.K. Gupta, Corrosion-resistant metallic coatings for aluminum alloys by cold spray, Corros. Sci. 209 (2022) 110720. https://doi.org/10.1016/J.CORSCI.2022.110720.

[22] Z. Sun, X. Tan, S.B. Tor, W.Y. Yeong, Selective laser melting of stainless steel 316L with low porosity and high build rates, Mater. Des. 104 (2016) 197–204. https://doi.org/10.1016/j.matdes.2016.05.035.

[23] B. AlMangour, D. Grzesiak, J.M. Yang, In situ formation of TiC-particle-reinforced stainless steel matrix nanocomposites during ball milling: Feedstock powder preparation for selective laser melting at various energy densities, Powder Technol. 326 (2018) 467–478. https://doi.org/10.1016/j.powtec.2017.11.064.

[24] T. Kurzynowski, K. Gruber, W. Stopyra, B. Kuźnicka, E. Chlebus, Correlation between process parameters, microstructure and properties of 316 L stainless steel processed by selective laser melting, Mater. Sci. Eng. A. 718 (2018) 64–73. https://doi.org/10.1016/j.msea.2018.01.103.

[25] W.M. Tucho, V.H. Lysne, H. Austbø, A. Sjolyst-Kverneland, V. Hansen, Investigation of effects of process parameters on microstructure and hardness of SLM manufactured SS316L, J. Alloys Compd. 740 (2018) 910–925. https://doi.org/10.1016/j.jallcom.2018.01.098.

[26] K. Saeidi, X. Gao, Y. Zhong, Z.J. Shen, Hardened austenite steel with columnar sub-grain structure formed by laser melting, Mater. Sci. Eng. A. 625 (2015) 221–229. https://doi.org/10.1016/j.msea.2014.12.018.

[27] V.B. Vukkum, J. Christudasjustus, A.A. Darwish, S.M. Storck, R.K. Gupta, Enhanced corrosion resistance of additively manufactured stainless steel by modification of feedstock, Npj Mater. Degrad. 6 (2022) 1–11. https://doi.org/10.1038/s41529-021-00215-z.

[28] Y. Zhong, L. Liu, S. Wikman, D. Cui, Z. Shen, Intragranular cellular segregation network structure strengthening 316L stainless steel prepared by selective laser melting, J. Nucl. Mater. 470 (2016) 170–178. https://doi.org/10.1016/j.jnucmat.2015.12.034.

[29] B. AlMangour, M.S. Baek, D. Grzesiak, K.A. Lee, Strengthening of stainless steel by titanium carbide addition and grain refinement during selective laser melting, Mater. Sci. Eng. A. 712 (2018) 812–818. https://doi.org/10.1016/j.msea.2017.11.126.

[30] O.O. Salman, C. Gammer, J. Eckert, M.Z. Salih, E.H. Abdulsalam, K.G. Prashanth, S. Scudino, Selective laser melting of 316L stainless steel: Influence of TiB2 addition on microstructure and mechanical properties, Mater. Today Commun. 21 (2019) 100615. https://doi.org/10.1016/j.mtcomm.2019.100615.

[31] S. Zhao, X. Shen, J. Yang, W. Teng, Y. Wang, Densification behavior and mechanical properties of nanocrystalline TiC reinforced 316L stainless steel composite parts fabricated by selective laser melting, Opt. Laser Technol. 103 (2018) 239–250. https://doi.org/10.1016/j.optlastec.2018.01.005.

[32] B. AlMangour, Y.K. Kim, D. Grzesiak, K.A. Lee, Novel TiB2-reinforced 316L stainless steel nanocomposites with excellent room- and high-temperature yield strength developed by additive manufacturing, Compos. Part B Eng. 156 (2019) 51–63. https://doi.org/10.1016/j.compositesb.2018.07.050.

[33] M.U.F. Khan, A. Patil, J. Christudasjustus, T. Borkar, R.K. Gupta, Spark plasma sintering of a high-energy ball milled Mg-10 wt% Al alloy, J. Magnes. Alloy. 8 (2020) 319–328. https://doi.org/10.1016/j.jma.2020.02.006.

[34] J. Christudasjustus, T. Larimian, J. Esquivel, S. Gupta, A.A. Darwish, T. Borkar, R.K. Gupta, Aluminum alloys with high elastic modulus, Mater. Lett. 320 (2022) 132292. https://doi.org/10.1016/j.matlet.2022.132292.

[35] J. Christudasjustus, C.S. Witharamage, G. Walunj, T. Borkar, R.K. Gupta, The influence of

spark plasma sintering temperatures on the microstructure, hardness, and elastic modulus of the nanocrystalline Al-xV alloys produced by high-energy ball milling, J. Mater. Sci. Technol. 122 (2022) 68–76. https://doi.org/10.1016/j.jmst.2022.02.008.

[36] L. Esteves, J. Christudasjustus, S.P. O'Brien, C.S. Witharamage, A.A. Darwish, G. Walunj, P. Stack, T. Borkar, R.E. Akans, R.K. Gupta, Effect of V content on corrosion behavior of high-energy ball milled AA5083, Corros. Sci. 186 (2021) 109465. https://doi.org/10.1016/j.corsci.2021.109465.

[37] J. Christudasjustus, C.S. Witharamage, V.B. Vukkum, G. Walunj, T. Borkar, R.K. Gupta, Surface Film Formation on Al-V Alloys with Far-From-Equilibrium Microstructure, J. Electrochem. Soc. 170 (2023) 031508. https://doi.org/10.1149/1945-7111/acc7ce.

[38] J. Christudasjustus, V.B. Vukkum, R.K. Gupta, Evolution of surface film in AA2024-T3 after a long-term immersion in NaCl solution, Corros. Sci. 215 (2023) 111056. https://doi.org/10.1016/J.CORSCI.2023.111056.

[39] X. Yin, Q. Zhai, Q. Zhang, K. Wang, L. Meng, Z. Ma, G. Chen, S. Wang, L. Wang, Effect of tungsten particles on microstructure and properties of 316 L stainless steel manufactured by selective laser melting, J. Manuf. Process. 68 (2021) 210–221. https://doi.org/10.1016/J.JMAPRO.2021.05.039.

[40] J. Quan, K. Lin, D. Gu, Selective laser melting of silver submicron powder modified 316L stainless steel: Influence of silver addition on microstructures and performances, Powder Technol. 364 (2020) 478–483. https://doi.org/10.1016/j.powtec.2020.01.082.

[41] H. Yin, J. Yang, Y. Zhang, L. Crilly, R.L. Jackson, X. Lou, Carbon nanotube (CNT) reinforced 316L stainless steel composites made by laser powder bed fusion: Microstructure and wear response, Wear. 496–497 (2022) 204281. https://doi.org/10.1016/j.wear.2022.204281.

[42] A. Nieto, V.B. Vukkum, P. Jalagam, K. Nema, J. Budan, R.K. Gupta, T.Y. Ansell, 3D printed carbon nanotube reinforced stainless steel via selective laser melting, MRS Commun. 12 (2022) 578–584. https://doi.org/10.1557/s43579-022-00200-w.

[43] Y. Han, Y. Zhang, H. Jing, D. Lin, L. Zhao, L. Xu, P. Xin, Selective laser melting of low-content graphene nanoplatelets reinforced 316L austenitic stainless steel matrix: Strength enhancement without affecting ductility, Addit. Manuf. 34 (2020) 101381. https://doi.org/10.1016/J.ADDMA.2020.101381.

[44] V.B. Vukkum, F. Ozdemir, S. Storck, R.K. Gupta, Corrosion performance of feedstock modified – Additively manufactured stainless steel, Corros. Sci. 209 (2022) 110724. https://doi.org/10.1016/J.CORSCI.2022.110724.

[45] O. Salman, A. Funk, A. Waske, J. Eckert, S. Scudino, Additive Manufacturing of a 316L Steel Matrix Composite Reinforced with CeO2 Particles: Process Optimization by Adjusting the Laser Scanning Speed, Technologies. 6 (2018) 25. https://doi.org/10.3390/technologies6010025.

[46] W. Zhai, W. Zhou, S.M.L. Nai, J. Wei, Characterization of nanoparticle mixed 316 L powder for additive manufacturing, J. Mater. Sci. Technol. 47 (2020) 162–168. https://doi.org/10.1016/j.jmst.2020.02.019.

[47] S.R. Oke, O.O. Ige, O.E. Falodun, A.M. Okoro, M.R. Mphahlele, P.A. Olubambi, Influence of TiN nanoparticle addition on microstructure and properties of Fe22Cr alloy fabricated by spark plasma sintering, Int. J. Adv. Manuf. Technol. 103 (2019) 4529–4540. https://doi.org/10.1007/s00170-019-03873-1.

[48] M.B. Wilms, R. Streubel, F. Frömel, A. Weisheit, J. Tenkamp, F. Walther, S. Barcikowski, J.H. Schleifenbaum, B. Gökce, Laser additive manufacturing of oxide dispersion strengthened steels using laser-generated nanoparticle-metal composite powders, Procedia CIRP. 74 (2018) 196–200. https://doi.org/10.1016/j.procir.2018.08.093.

[49] T. Horn, C. Rock, D. Kaoumi, I. Anderson, E. White, T. Prost, J. Rieken, S. Saptarshi, R. Schoell, M. DeJong, S. Timmins, J. Forrester, S. Lapidus, R. Napolitano, D. Zhang, J. Darsell, Laser powder bed fusion additive manufacturing of oxide dispersion strengthened steel using gas atomized reaction synthesis powder, Mater. Des. 216 (2022) 110574. https://doi.org/10.1016/J.MATDES.2022.110574.

[50] S. Srisawadi, D. Tanprayoon, Y. Sato, M. Tsukamoto, T. Suga, Fabrication of 316L stainless steel with TiN addition by vacuum laser powder bed fusion, Opt. Laser Technol. 126 (2020) 106116. https://doi.org/10.1016/j.optlastec.2020.106116.

[51] B. AlMangour, D. Grzesiak, J.M. Yang, In-situ formation of novel TiC-particle-reinforced 316L stainless steel bulk-form composites by selective laser melting, J. Alloys Compd. 706 (2017) 409–418. https://doi.org/10.1016/j.jallcom.2017.01.149.

[52] F. Ozdemir, J. Christudasjustus, V.B. Vukkum, H. Okuyucu, R.K. Gupta, Need of an Inert Atmosphere for High-Energy Ball Milling of Al Alloys, J. Mater. Eng. Perform. 32 (2022)

3007–3013. https://doi.org/10.1007/s11665-022-07309-y.

[53] F. Ozdemir, C.S. Witharamage, J. Christudasjustus, A. Darwish, H. Okuyucu, R.K. Gupta, Corrosion behavior of a bulk nanocrystalline Al-Fe alloy, Corros. Sci. 209 (2022) 110727. https://doi.org/10.1016/J.CORSCI.2022.110727.

[54] J. Christudasjustus, M.R. Felde, C.S. Witharamage, J. Esquivel, A.A. Darwish, C. Winkler, R.K. Gupta, Age-hardening behavior, corrosion mechanisms, and passive film structure of nanocrystalline Al-V supersaturated solid solution, J. Mater. Sci. Technol. 135 (2023) 1–12. https://doi.org/10.1016/j.jmst.2022.06.044.

[55] Q. Chao, V. Cruz, S. Thomas, N. Birbilis, P. Collins, A. Taylor, P.D. Hodgson, D. Fabijanic, On the enhanced corrosion resistance of a selective laser melted austenitic stainless steel, Scr. Mater. 141 (2017) 94–98. https://doi.org/10.1016/j.scriptamat.2017.07.037.

[56] R. Ke, R. Alkire, Surface analysis of corrosion pits initiated at MnS inclusions in 304 stainless steel, J. Electrochem. Soc. 139 (1992) 1573–1580. https://doi.org/10.1149/1.2069458.

[57] R. Ke, R. Alkire, Initiation of corrosion pits at inclusions on 304 stainless steel, J. Electrochem. Soc. 142 (1995) 4056. https://doi.org/10.1149/1.2048462.

[58] V. Cruz, Q. Chao, N. Birbilis, D. Fabijanic, P.D. Hodgson, S. Thomas, Electrochemical studies on the effect of residual stress on the corrosion of 316L manufactured by selective laser melting, Corros. Sci. 164 (2020) 108314. https://doi.org/10.1016/J.CORSCI.2019.108314.

[59] P. Deng, M. Karadge, R.B. Rebak, V.K. Gupta, B.C. Prorok, X. Lou, The origin and formation of oxygen inclusions in austenitic stainless steels manufactured by laser powder bed fusion, Addit. Manuf. 35 (2020) 101334. https://doi.org/10.1016/j.addma.2020.101334.

[60] D. Kong, C. Dong, S. Wei, X. Ni, L. Zhang, R. Li, L. Wang, C. Man, X. Li, About metastable cellular structure in additively manufactured austenitic stainless steels, Addit. Manuf. 38 (2021) 101804. https://doi.org/10.1016/j.addma.2020.101804.

[61] Y. Zhong, L. Liu, J. Zou, X. Li, D. Cui, Z. Shen, Oxide dispersion strengthened stainless steel 316L with superior strength and ductility by selective laser melting, J. Mater. Sci. Technol. 42 (2020) 97–105. https://doi.org/10.1016/j.jmst.2019.11.004.

[62] M.J.K. Lodhi, A.D. Iams, E. Sikora, T.A. Palmer, Microstructural features contributing to macroscopic corrosion: The role of oxide inclusions on the corrosion properties of

additively manufactured 316L stainless steel, Corros. Sci. 203 (2022). https://doi.org/10.1016/j.corsci.2022.110354.

[63] D. Kong, C. Dong, X. Ni, L. Zhang, J. Yao, C. Man, X. Cheng, K. Xiao, X. Li, Mechanical properties and corrosion behavior of selective laser melted 316L stainless steel after different heat treatment processes, J. Mater. Sci. Technol. 35 (2019) 1499–1507. https://doi.org/10.1016/j.jmst.2019.03.003.

[64] D. Riabov, A. Leicht, J. Ahlström, E. Hryha, Investigation of the strengthening mechanism in 316L stainless steel produced with laser powder bed fusion, Mater. Sci. Eng. A. 822 (2021) 141699. https://doi.org/10.1016/J.MSEA.2021.141699.

[65] G. Sander, S. Thomas, V. Cruz, M. Jurg, N. Birbilis, X. Gao, M. Brameld, C.R. Hutchinson, On the corrosion and metastable pitting characteristics of 316L stainless steel produced by selective laser melting, J. Electrochem. Soc. 164 (2017) C250–C257. https://doi.org/10.1149/2.0551706jes.

[66] Z. Duan, C. Man, C. Dong, Z. Cui, D. Kong, L. Wang, X. Wang, Pitting behavior of SLM 316L stainless steel exposed to chloride environments with different aggressiveness: Pitting mechanism induced by gas pores, Corros. Sci. 167 (2020) 108520. https://doi.org/10.1016/j.corsci.2020.108520.

[67] C. Man, C. Dong, T. Liu, D. Kong, D. Wang, X. Li, The enhancement of microstructure on the passive and pitting behaviors of selective laser melting 316L SS in simulated body fluid, Appl. Surf. Sci. 467–468 (2019) 193–205. https://doi.org/10.1016/j.apsusc.2018.10.150.

[68] C.L. Wu, S. Zhang, C.H. Zhang, J.B. Zhang, Y. Liu, J. Chen, Effects of SiC content on phase evolution and corrosion behavior of SiC-reinforced 316L stainless steel matrix composites by laser melting deposition, Opt. Laser Technol. 115 (2019) 134–139. https://doi.org/10.1016/j.optlastec.2019.02.029.

[69] G. Sander, D. Jiang, Y. Wu, N. Birbilis, Exploring the possibility of a stainless steel and glass composite produced by additive manufacturing, Mater. Des. 196 (2020) 109179. https://doi.org/10.1016/j.matdes.2020.109179.

[70] R.K. Gupta, N. Birbilis, The influence of nanocrystalline structure and processing route on corrosion of stainless steel: A review, Corros. Sci. 92 (2015) 1–15. https://doi.org/10.1016/j.corsci.2014.11.041.

[71] Standard Test Methods for Determination of Carbon, Sulfur, Nitrogen, and Oxygen in Steel

and in Steel, Iron, Nickel, and Cobalt Alloys by Various Combustion and Fusion Techniques, 2011. https://doi.org/10.1520/E1019-18.2.

[72] A262-14 Standard Practices for Detecting Susceptibility to Intergranular Attack in Austenitic Stainless Steels, 2015. https://doi.org/10.1520/A0262-14.

[73] M.J. Paul, Q. Liu, J.P. Best, X. Li, J.J. Kruzic, U. Ramamurty, B. Gludovatz, Fracture resistance of AlSi10Mg fabricated by laser powder bed fusion, Acta Mater. 211 (2021) 116869. https://doi.org/10.1016/J.ACTAMAT.2021.116869.

[74] G. Wang, H. Ouyang, C. Fan, Q. Guo, Z. Li, W. Yan, Z. Li, The origin of high-density dislocations in additively manufactured metals, Mater. Res. Lett. 8 (2020) 283–290. https://doi.org/10.1080/21663831.2020.1751739.

[75] H. Ezuber, A. Alshater, M. Abulhasan, Role of thiosulfate in susceptibility of AISI 316L austenitic stainless steels to pitting corrosion in 3.5% sodium chloride solutions, Surf. Eng. Appl. Electrochem. 53 (2017) 493–500. https://doi.org/10.3103/S1068375517050052.

[76] A. Munis, M. Zheng, T. Zhao, Effect of sulfate and meta-silicate ions on pitting corrosion of stainless steel-316 in chloride containing simulated coal gasifier aqueous effluents, Mater. Res. Express. 6 (2019) 076541. https://doi.org/10.1088/2053-1591/AB160E.

[77] T.L.S.L. Wijesinghe, D.J. Blackwood, Real time pit initiation studies on stainless steels: The effect of sulphide inclusions, Corros. Sci. 49 (2007) 1755–1764. https://doi.org/10.1016/j.corsci.2006.10.025.

[78] N. Hara, K. Hirabayashi, Y. Sugawara, I. Muto, Improvement of Pitting Corrosion Resistance of Type 316L Stainless Steel by Potentiostatic Removal of Surface MnS Inclusions, Int. J. Corros. 2012 (2012). https://doi.org/10.1155/2012/482730.

[79] T. Voisin, R. Shi, Y. Zhu, Z. Qi, M. Wu, S. Sen-Britain, Y. Zhang, S.R. Qiu, Y.M. Wang, S. Thomas, B.C. Wood, Pitting Corrosion in 316L Stainless Steel Fabricated by Laser Powder Bed Fusion Additive Manufacturing: A Review and Perspective, JOM. 74 (2022) 1668–1689. https://doi.org/10.1007/s11837-022-05206-2.

[80] R.K. Gupta, N.L. Sukiman, M.K. Cavanaugh, B.R.W. Hinton, C.R. Hutchinson, N. Birbilis, Metastable pitting characteristics of aluminium alloys measured using current transients during potentiostatic polarisation, Electrochim. Acta. 66 (2012) 245–254. https://doi.org/10.1016/j.electacta.2012.01.090.

[81] R.K. Gupta, A. Deschamps, M.K. Cavanaugh, S.P. Lynch, N. Birbilis, Relating the Early

Evolution of Microstructure with the Electrochemical Response and Mechanical Performance of a Cu-Rich and Cu-Lean 7xxx Aluminum Alloy, J. Electrochem. Soc. 159 (2012) C492–C502. https://doi.org/10.1149/2.062211JES/XML.

[82] K.D. Ralston, N. Birbilis, M.K. Cavanaugh, M. Weyland, B.C. Muddle, R.K.W. Marceau, Role of nanostructure in pitting of Al-Cu-Mg alloys, Electrochim. Acta. 55 (2010) 7834–7842. https://doi.org/10.1016/j.electacta.2010.02.001.

[83] K.D. Ralston, N. Birbilis, M. Weyland, C.R. Hutchinson, The effect of precipitate size on the yield strength-pitting corrosion correlation in Al-Cu-Mg alloys, (n.d.). https://doi.org/10.1016/j.actamat.2010.07.010.

[84] R.I. Revilla, M. Van Calster, M. Raes, G. Arroud, F. Andreatta, L. Pyl, P. Guillaume, I. De Graeve, Microstructure and corrosion behavior of 316L stainless steel prepared using different additive manufacturing methods: A comparative study bringing insights into the impact of microstructure on their passivity, Corros. Sci. 176 (2020) 108914. https://doi.org/10.1016/J.CORSCI.2020.108914.

[85] D. Kong, C. Dong, X. Ni, L. Zhang, H. Luo, R. Li, L. Wang, C. Man, X. Li, The passivity of selective laser melted 316L stainless steel, Appl. Surf. Sci. 504 (2020) 144495. https://doi.org/10.1016/j.apsusc.2019.144495.